Geophysical Research Letters

Supporting Information for

A Thermal Origin for Most Marsquakes

Lei Zhang[1, 2], Jinhai Zhang[1, 2, 3*], Ross N. Mitchell[4,5*], Peng Cao[6], Jihang Liu[7]

[1] Key Laboratory of Earth and Planetary Physics, Institute of Geology and Geophysics, Chinese Academy of Sciences, Beijing, China
[2] Innovation Academy for Earth Science, Chinese Academy of Sciences, Beijing, China
[3] College of Earth and Planetary Sciences, University of Chinese Academy of Sciences, Beijing, China
[4] State Key Laboratory of Lithospheric Evolution, Institute of Geology and Geophysics, Chinese Academy of Sciences, Beijing, China
[5] University of Chinese Academy of Sciences, Beijing, China
[6] College of Architecture and Civil Engineering, Beijing University of Technology, Beijing, China
[7] College of Control Science and Engineering, Bohai University, Jinzhou, Liaoning Province, China

Contents of this file

Introduction

Text S1 gives the solution of 1D heat conduction equation.
Text S2 shows the process of the temperature correction from the air to the ground.
Text S3 analyses the results of the subsurface heat conduction beneath InSight.
Figure S1 presents the correction process from the air temperature to ground temperature.
Figure S2 shows the annually averaged heat conduction model of the subsurface under the InSight landing site.
Figure S3 shows the temperature as a function of both time of day and mission days (sol) at top 10 cm of the subsurface.
Figure S4 shows phase arrival times of the 6 types of marsquake events and their histogram.
Figure S5 shows the rates of temperature change at different depths at 18:00 LMST.
Figure S6 shows histograms of the 6 marsquake types in an entire Martian year.
Figure S7 gives the simulated ground motion at the receiver of seismic waves in sol 226.
Table S1 presents the detailed numbers of the marsquake events.

Text S1. Solution of 1D heat conduction equation

Surface heat flow estimation provides constraints on the distribution of heat producing radioisotopes and the rate of mantle convection [Barlow, 2014]. In regions where conduction dominates, heat flux (Q) is related to the thermal gradient ($\partial T/\partial z$) by Fourier's Law

$$Q = k\left(\frac{\partial T}{\partial z}\right),$$

where T is temperature and z is depth (downward positive). The thermal conductivity (k) is related to the density (ρ), specific heat (c), and thermal diffusivity (κ) of the ground as below

$$k = \rho c \kappa.$$

The rate at which layers of ground gain or lose heat can be given by

$$\rho c \frac{\partial T}{\partial t} = \frac{\partial Q}{\partial z}.$$

Thus, we can get the heat conduction equation as below

$$\frac{\partial T}{\partial t} = \kappa \frac{\partial^2 T}{\partial^2 z},$$

where $T(z, t)$ is a function of depth (z) and time (t). On the ground surface ($z = 0$), $T(0, t)$ can be described as a sine function

$$T(0,t) = T_0 + A_0 \sin\left(\frac{2\pi}{P}t + \varphi_0\right),$$

where P is the period, T_0 is the average ground temperature in the period, A_0 is the amplitude, and φ_0 is the initial phase. Then the heat conduction equation can be solved as

$$T(z,t) = T_0 + \gamma z + A_0\, e^{-\sqrt{\frac{\pi}{\kappa P}}z} \sin\left(\frac{2\pi}{P}t + \varphi_0 - \sqrt{\frac{\pi}{\kappa P}}z\right),$$

where γ is a constant to describe the vertical gradient of the average temperature, which can be assumed as 0 in regions with low heat flow. At InSight landing site, the heat flow is estimated to be 18 mWm^{-2} [Parro *et al.*, 2017], extremely lower than the heat flow from the solar irradiation. Thus, for simplicity, we assume $\gamma = 0$ in this study.

Since the ground temperature $T(0, t)$ is generally not a perfect sine function, we can replace it by sine series expansion

$$T(0,t) = T_0 + \sum_{i=1}^{n} A_{0i} \sin\left(\frac{2i\pi}{P}t + \varphi_{0i}\right),$$

where i is the order of expansion. Thus, the heat conduction equation can be rewritten as

$$T(z,t) = T_0 + \sum_{i=1}^{n} A_{0i} e^{-\sqrt{\frac{i\pi}{\kappa P}}z} \sin\left(\frac{2i\pi}{P}t + \varphi_{0i} - \sqrt{\frac{i\pi}{\kappa P}}z\right),$$

where n is the number of orders, which is set as 9 in our simulation.

Text S2. Temperature Correction from the Air to the Ground

The air temperature sensors are on the deck of the InSight lander, ~1 m away from the ground. However, the input for the heat conduction simulation is the ground temperature, usually hotter in the daily time and cooler in the nighttime than the air temperature at the altitude of ~1 m. We correct the air temperature (altitude = 1 m) to the ground temperature (altitude = 0 m) according to the modeled air temperature and ground temperature from the Martian Climate Database [Forget *et al.*, 1999] as below:

$$T_{ground}^{\text{Estimated}} = T_{air}^{Recorded} \frac{T_{ground}^{MCD}}{T_{air}^{MCD}},$$

where $T_{ground}^{Estimated}$ is the estimated ground temperature, which is used as temperature boundary for the heat conduction simulation; $T_{air}^{Recorded}$ is the air temperature recorded by InSight; T_{ground}^{MCD} and T_{air}^{MCD} are the ground (altitude = 0 m) and the air (altitude = 1 m) temperatures modeled from MCD, respectively.

Figures S1a and S1b present the MCD temperature as a function of both Solar longitude (Ls) and Local Mean Solar Time (LMST) in the air (altitude = 1 m) and on the ground (altitude = 0 m), respectively. Figures S1c presents an example of the temperature correction for sol 400. Similarly, we estimate the ground temperature sol by sol in all the sols with entire-sol continuous temperature records (Figure S1d).

Text S3. Results of the Subsurface Heat Conduction Beneath InSight

As mentioned in Text S1, the heat conduction equation can describe the thermal process of a given model with several controlling parameters. In our numerical calculations, we use typical values of these parameters obtained from the heating experiments from HP^3 [*Grott et al.*, 2021] as follows: soil density ρ = 1211 kg m^{-3}, specific heat c = 630 J kg^{-1} K^{-1}, and thermal conductivity k = 0.039 W m^{-1} K^{-1}. Thus, the thermal diffusivity $\kappa = k/(\rho c)$ at the InSight landing site can be estimated as 5.1×10^{-8} m^2 s^{-1}.

Figure S2a shows the complete numerical solution of daily temperature variation with depth, given the annual average daily temperature as the temperature boundary at $z = 0$. The magnitude of temperature variation decreases with increasing depth at any given time (Figure S2b). The highest subsurface temperature arises with a varying time delay at different depths (Figure S2c). Below the depth of 25 cm (Figure S2b), the temperature is almost stable (i.e., insensitive to heat conduction from solar forcing). This indicates that we can focus on the shallowest 25 cm for analyzing the diurnal variations of subsurface temperature, especially for the shallowest 10 cm, below which daily temperature variations are less than 15 K.

We can see that at the depth of 0 cm (Figure S3a), the temperature starts to rise at 06:00–08:00 and then starts to drop at 17:00–19:00. At the depth of 2 cm (Figure S3b), the temperature starts to rise at 08:00–12:00 and drop at 18:00–20:00. The time delays become larger with increasing depth (Figures S3c-f). Meanwhile, the duration of peak temperature periods (purple) become shorter with depth. The temperature is nearly stable at the depth of 10 cm (Figure S3f) and is totally invariant at the depth of 25 cm (Figure S1b).

Figure S1

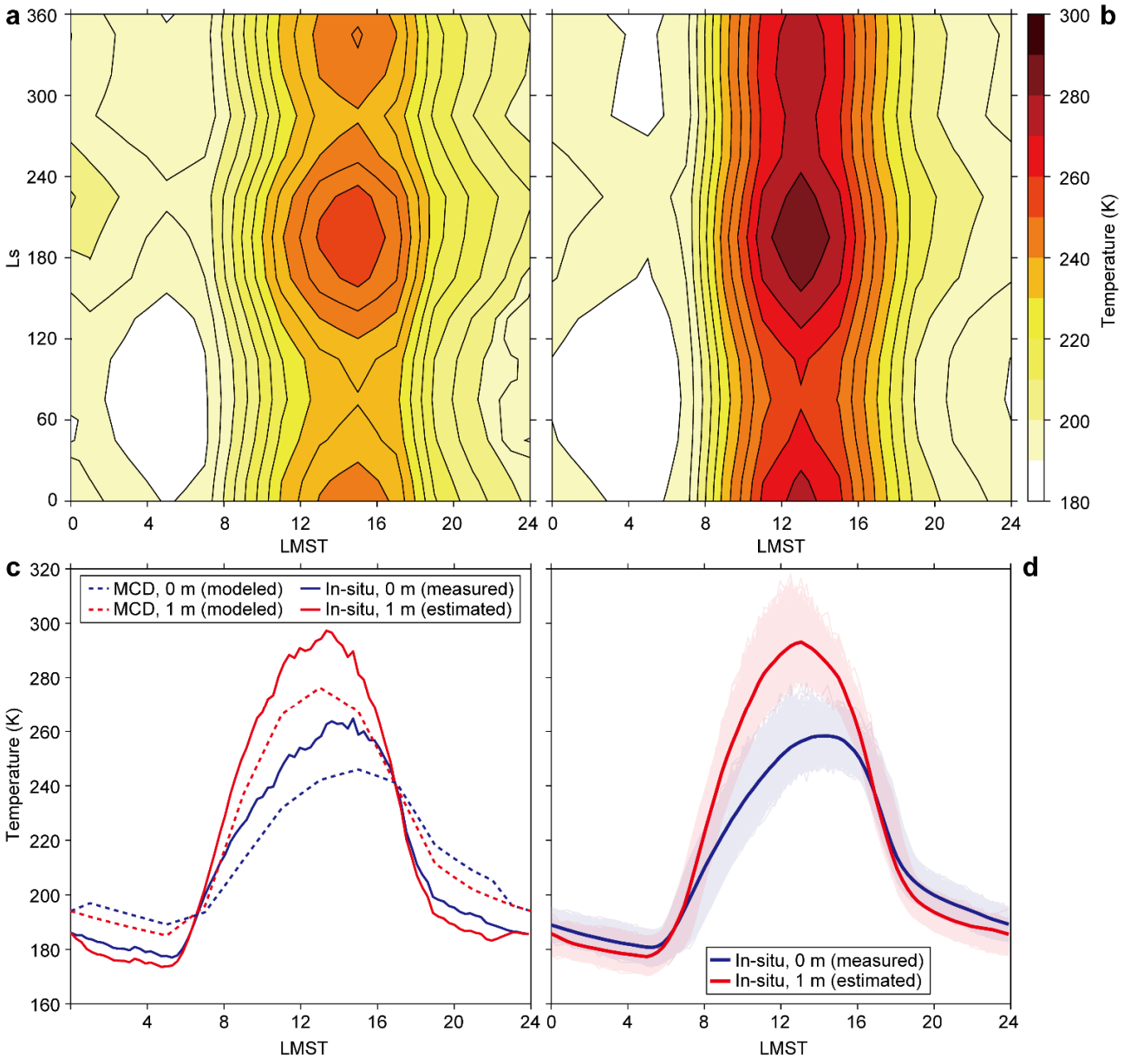

Figure S1. The correction process from air temperature to ground temperature. (a) Air temperature (altitude = 1 m) from MCD. (b) Ground temperature (altitude = 0 m) from MCD. (c) An example of the temperature correction for sol 400. (d) The InSight recorded air temperature (altitude = 1 m) and the estimated ground temperature (altitude = 0 m) after the correction process. The temperature records (semi-transparent blue lines) from the BOOM-Y component of the TWINS (Temperature and Winds for InSight) tip sensor [Spiga et al., 2018] is used in our analysis. Only the sols with entire-sol continuous temperature records are considered. The red and dark blue solid lines denote the average temperatures of these sols, together with the daily records (semi-transparent lines).

Figure S2

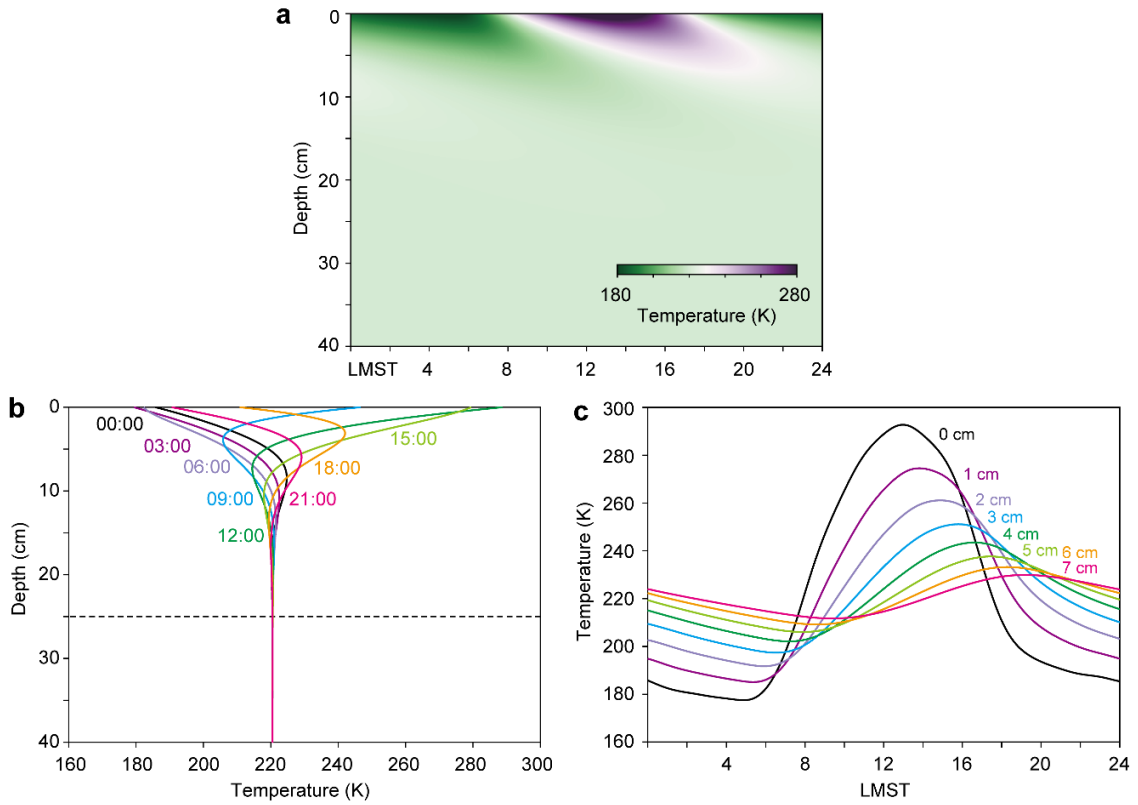

Figure S2. Annually average temperature of the subsurface under the InSight landing site. (a) Temperature as a function of both depth and time of a sol. (b) Temperature as a function of depth at different times of a day. (c) Daily temperature fluctuations at different depths.

Figure S3

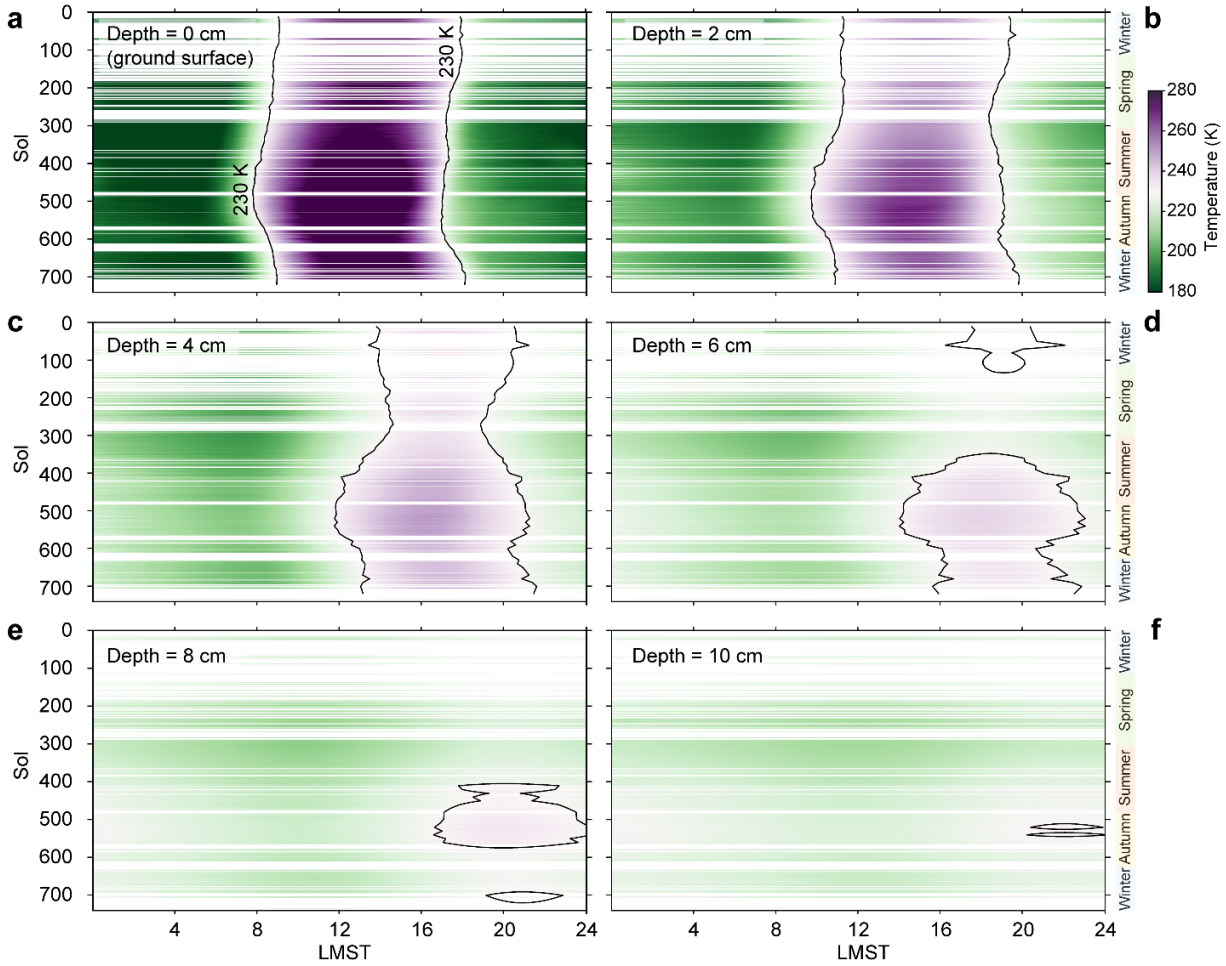

Figure S3. Temperature as a function of both time of day and mission days (sol) at top 10 cm of the subsurface. Horizontal white spaces indicate data gaps due to solar conjunctions or machine stoppages. Black lines denote the isolines of 230 K.

Figure S4

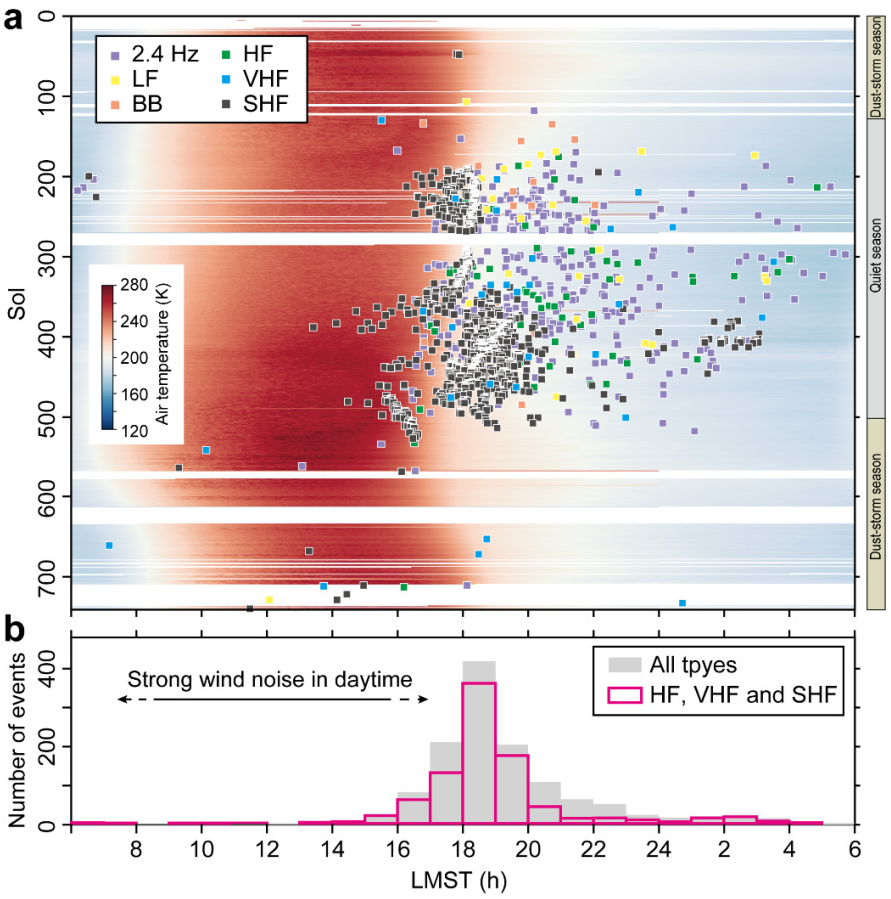

Figure S4. **Phase arrival times of the 6 types of marsquake events and their histogram.** (a) Phase arrival times of the 6 types of marsquake events: 2.4 Hz, broadband (BB), low frequency (LF), high frequency (HF), very high frequency (VHF), and super high frequency (SHF). The background color spectrum is the air temperature centered at sunset. (b) Histogram of marsquake events.

Figure S5

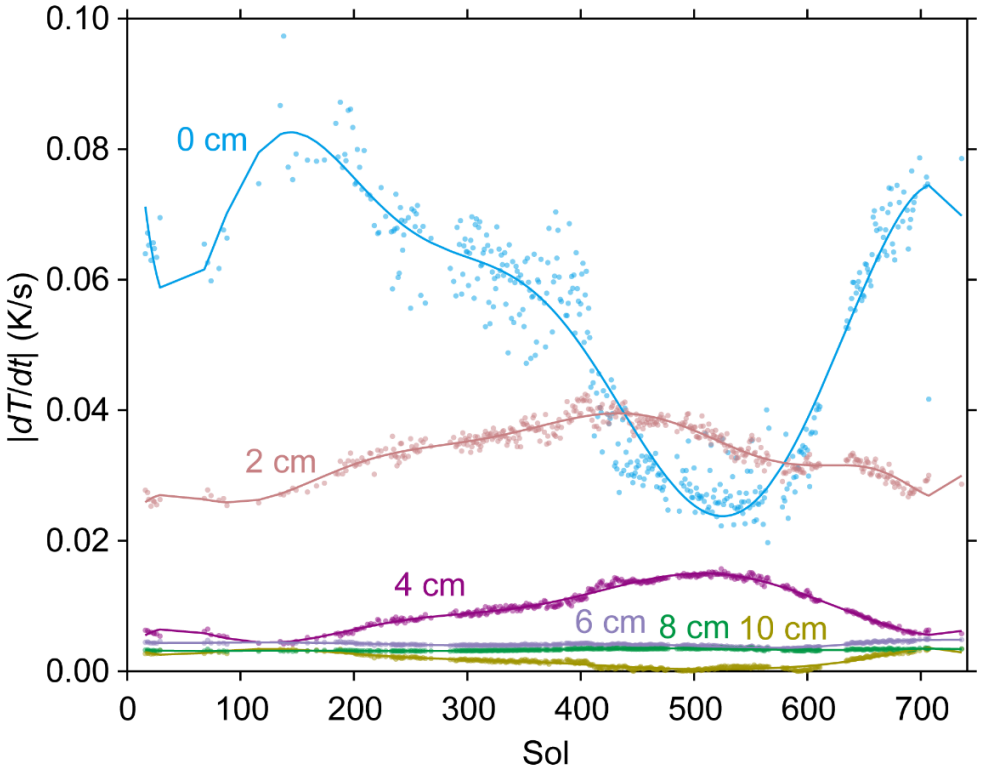

Figure S5. **Calculated absolute temperature variations at different depths on 18:00 LMST.** The dots are calculated values, and the lines are the fitting results.

Figure S6

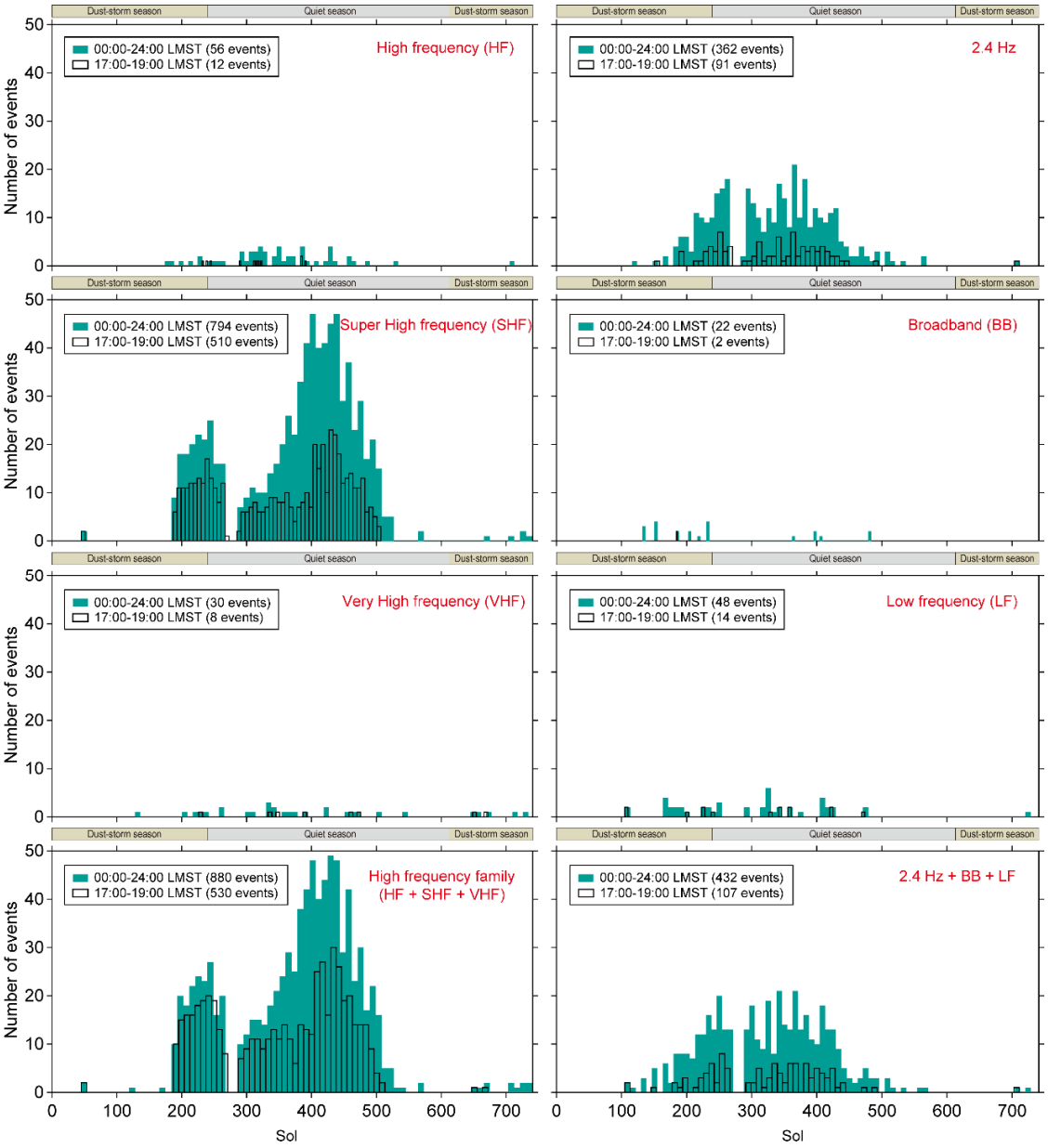

Figure S6. Histograms of the 6 types of marsquake events [*InSight Marsquake Service*, 2021]. Green filled and black framed bars indicate events during 00:00–24:00 and 17:00–19:00 LMST, respectively. Magenta text denotes the types of marsquakes.

Figure S7

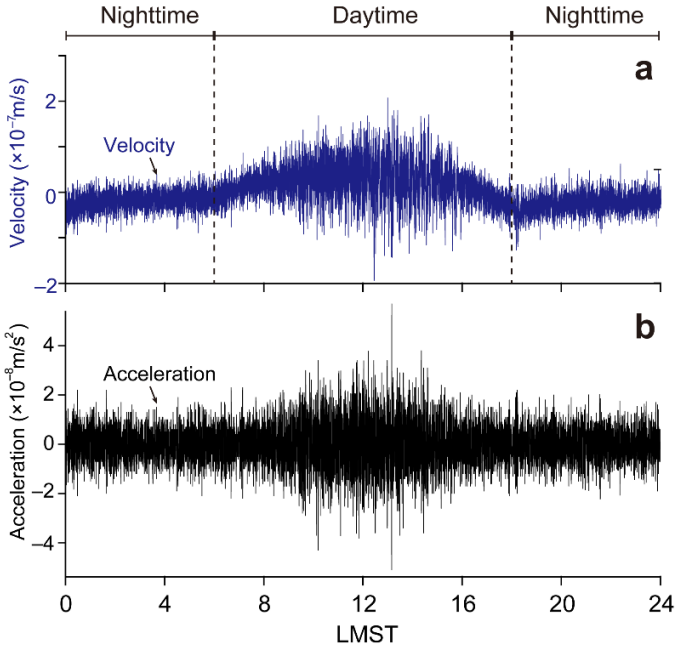

Figure S7. The simulated ground motion at the receiver of seismic waves in sol 226. (a) Vertical velocity. (b) Vertical acceleration.

Table S1. Numbers of different marsquake types [*InSight Marsquake Service*, 2021].

Types	00:00-24:00 (A)	17:00-19:00 (B)	16:00-20:00 (C)	B/A*100%	C/A*100%
High frequency (HF)	56	12	22	21.4%	39.3%
Super high frequency (SHF)	794	510	692	64.2%	87.2%
Very high frequency (VHF)	30	8	14	26.7%	46.7%
2.4 Hz	362	91	157	25.1%	43.4%
Broadband (BB)	22	2	12	9.1%	54.5%
Low frequency (LF)	48	14	21	29.2%	43.8%
HF + SHF + VHF	880	530	728	60.2%	82.7%
2.4 Hz + BB + LF	432	107	190	24.8%	44.0%
HF + SHF + VHF + 2.4 Hz + BB + LF	1312	637	918	48.6%	70.0%

References

InSight Marsquake Service (2021). Mars Seismic Catalogue, InSight Mission; V7 2021-07-01. ETHZ, IPGP, JPL, ICL, Univ. Bristol. https://doi.org/10.12686/a12.

Forget, F., F. Hourdin, R. Fournier, C. Hourdin, O. Talagrand, M. Collins, S. R. Lewis, P. L. Read, and J. P. Huot (1999), Improved general circulation models of the martian atmosphere from the surface to above 80 km, *Journal of Geophysical Research: Planets*, *104*(E10), 24155-24175.

Grott, M., T. Spohn, J. Knollenberg, C. Krause, T. L. Hudson, S. Piqueux, N. Müller, M. P. Golombek, C. Vrettos, and E. Marteau, et al., (2021), Thermal conductivity of the martian soil at the InSight landing site from HP^3 active heating experiments, *Journal of Geophysical Research: Planets*, 126(7), e2021JE006861.

Parro, L. M., Jiménez-Díaz, A., Mansilla, F. & Ruiz, J. Present-day heat flow model of Mars. *Scientific reports* **7**, 1–9 (2017).

Spiga, A., D. Banfield, N. A. Teanby, F. Forget, A. Lucas, B. Kenda, J. A. R. Manfredi, R. Widmer-Schnidrig, N. Murdoch, and M. T. Lemmon (2018), Atmospheric science with InSight, *Space Science Reviews*, *214*(7), 1-64.